Global Transport on a Spherical Multiple-Cell Grid

JIAN-GUO LI

Met Office, Exeter, United Kingdom

(Manuscript received 18 August 2009, in final form 31 August 2010)

ABSTRACT

Second- and third-order upstream nonoscillatory (UNO) advection schemes are applied on a spherical multiple-cell (SMC) grid for global transport. Similar to the reduced grid, the SMC grid relaxes the Courant–Friedrichs–Lewy (CFL) restriction of the Eulerian advection time step on the conventional latitude–longitude grid by zonally merging cells toward the poles. Round polar cells are introduced to remove the polar singularity of the spherical coordinate system. The unstructured feature of the SMC grid allows unused cells to be removed out of memory and transport calculations. Solid-body rotation and deformation flow tests are used for comparison with other transport schemes. Application on the global ocean surface is used to demonstrate the flexibility of the SMC grid by removing all land points and making possible the extension of global ocean surface wave models to cover the Arctic in response to the retreating sea ice in recent summers. Numerical results suggest that UNO schemes on the SMC grid are suitable for global transport.

1. Introduction

Transport is a physical process essential to all geofluid models, including atmospheric and oceanic models, as well as environmental tracer models. For global models, the standard latitude–longitude grid has historically been preferred for its simplicity and traditional mapping convention. However, the latitude–longitude grid is associated with a well-known ''polar problem'' or polar singularity, which is caused by the diminishing zonal grid size toward the poles. The polar problem of the latitude–longitude grid manifests itself in two effects on global transport. First, the diminishing grid length at high latitude exerts a rigorous time-step limit on Eulerian advection schemes as they are subject to the Courant–Friedrichs–Lewy (CFL) stability criterion, which requires the flow distance within one time step to be less than one grid length. The other effect is the singularity at the poles due to the collapse of the directional dimension. As a result, the conventional geophysical velocity (with u denoting the zonal velocity component and v the meridional) is no longer defined at the poles. The polar singularity is a purely mathematical problem; that is, it does not represent a physical singularity. Nevertheless, it prevents direct application of differential equations and definition of directional variables at the poles.

There are various approaches to tackling the polar problem in conventional latitude–longitude grids. One approach is to use semi-Lagrangian (SL) schemes to avoid the CFL restriction, as in Robert et al. (1985), Nair and Machenhauer (2002), and Zerroukat et al. (2004). Another is to zonally merge cells to increase the effective grid length for Eulerian schemes (Williamson and Browning 1973). Both the expanded polar zone (Prather et al. 1987; Li and Chang 1996) and reduced grid (Rasch 1994) techniques fall in the latter category. The reduced grid is similar to the adaptive mesh refinement (AMR) technique (Berger and Oliger 1984) except that only the zonal grid size is varied in the reduced grid. Hubbard and Nikiforakis (2003) use an AMR grid on the sphere with a weighted-average flux (WAF) finite-volume advection scheme. Jablonowski et al. (2006) introduce a block-structured AMR grid, which uses the reduced grid in the polar regions. Each block resembles a regular AMR grid, and different blocks are linked up through boundary (ghost) cells.

A common feature of these reduced and AMR latitude–longitude grids is the use of triangular cells around the poles. Finite-difference advection schemes on these latitude–longitude grids have suppressed the meridional fluxes through the polar vertices of these triangular cells because the face areas of these vertices are zero (e.g.,

Corresponding author address: Dr Jian-Guo Li, Met Office, FitzRoy Road, Exeter EX1 3PB, United Kingdom.
E-mail: jian-guo.li@metoffice.gov.uk

DOI: 10.1175/2010MWR3196.1

Rasch 1994). As a result, cross-pole transport is partially blocked due to the omission of these polar fluxes. Imagining each cell as a floating vessel, the advective transport may be viewed as displacement of the vessel in the flow direction from its fixed mesh position. For a crossing-pole flow, the upstream triangular cell is moved over the pole and it overlaps with all the fixed triangular meshes around the pole. Its flux into each fixed triangular mesh should then be proportional to its overlapping area with the fixed mesh. This implies that the flux from the upstream triangular cell into the downstream triangular cell directly across the pole should not be zero. This nonzero flux is, however, unachievable by the finite-difference scheme because fluxes between the opposite triangular cells are through the triangular vertices and are always zero. As a result, the triangular vessels can only turn around the pole by the zonal fluxes into neighboring cells as if there is a pin nailed at the pole to prevent the vessels from crossing it. Some transport schemes based on remapping the displaced cell, such as SL schemes, can simulate this cross-pole transport correctly and hence avoid the partial blocking on these latitude–longitude grids.

There are also various approaches for avoiding the polar problem that use nonconventional grids. These include the finite-element method with unstructured triangular cells (Hanert et al. 2004), the quasi-uniform spherical grid with quadrilaterals (Sadourny 1972), the geodesic grid with pentagons and hexagons (Lipscomb and Ringler 2005), and the conformal octagon approach (Purser and Rancic 1997). These nonconventional grids involve irregular cell shapes, and transport on these grids requires nonuniform interpolations and is known to be more expensive than finite-difference schemes on regular grids. The spherical grid proposed by Kurihara (1965) is quite similar to the reduced latitude–longitude grid. It relaxes the zonal cell size by gradually reducing the number of cells with increasing latitude. The resulting cells are no longer aligned along the meridians, so the finite-differencing has to be modified with nonuniform interpolations. This quasi-uniform grid is used in one ocean surface wave model (Janssen 2004). Kageyama and Sato (2004) combine the standard latitude–longitude grid with a perpendicularly rotated grid to replace the polar regions in one grid with the tropical regions in the other, resulting in a so called yin–yang (YY) grid. Links between the yin and yang grids are achieved through boundary conditions in their overlapping zones. Li et al. (2008) demonstrated global transport on the YY grid with a constrained interpolation profile–multimoment (CIP–MM) advection scheme, which is a mixture of SL and finite-volume methods.

In addition to the problem of polar singularities preventing the definition of vector variables at the poles, other difficulties in treating vector variables arise in the latitude–longitude grid due to the increased curvature of the parallels at high latitudes. For instance, in SL schemes, it becomes difficult to trace the starting point in the polar region. McDonald and Bates (1989) applied rotated grids in the polar region to avoid this problem. In ocean surface wave models, the wave energy spectrum is discretized into directional components relative to the local east (Tolman et al. 2002). Each directional component is stored in one directional bin and is treated as a scalar; that is, the spectral component is transported into the corresponding bin at the downstream grid point. This scalar assumption is a good approximation at low latitudes and is refined by a great circle turning term poleward as ocean waves travel along great circles. However, it becomes erroneous at high latitudes since the change of bin direction grows too large to be ignored if a reduced grid is used. For instance, if energy from one directional bin is propagated across the pole, its direction will be completely opposite to that of the same directional bin at the arrival point. The scalar assumption prevents the extension of ocean surface wave models to those portions of the Arctic Ocean that have been exposed due to retreating of the sea ice in recent summers.

Dynamical models on reduced latitude–longitude grids suffer from the same scalar assumption problem at high latitudes if their horizontal velocity components are defined relative to the local east and north. For instance, on a reduced grid corresponding to a 64×128 latitude–longitude grid, there are only 4 triangular cells around each pole. The local east changes 90° from one triangular cell to the next. This means that the meridional component v in one triangular cell corresponds to the zonal component u in the next triangular cell. Finite-difference equations, which involve velocity components of neighboring cells in a scalar equation, no longer hold at high latitudes on the reduced grid. This is partially the reason why the reduced grid is not popular in dynamical models. Jablonowski et al. (2009) have concluded that the enhanced errors in their dynamical model on a reduced grid "are mainly generated in the velocity components in the polar regions due to the extreme curvature of curvilinear coordinates near the poles." This scalar assumption problem at high latitudes should be solved in a dynamical model before the model is implemented on a reduced grid.

Apart from the polar problem, another drawback of the conventional latitude–longitude grid for ocean surface wave models is the waste of transport computation on land points. Operational ocean surface wave models, such as those used by Golding (1983), WAMDI Group (1988), and Tolman et al. (2002), deal with hundreds of wave energy spectral components at each grid point, and each component must be transported at a different speed and direction. Although wave energy spectra are stored only at sea points in order to reduce storage, on the latitude–longitude grid they have to be expanded to the full grid (both sea and land points) before the transport calculation can be carried out with finite-difference advection schemes. At the end of the advection calculation, spectra at land points are discarded from memory to reduce storage. These expansion–compression operations and advection calculations at land points waste quite a lot of computing time in ocean wave models. It is possible to suspend the calculation on land points by masking the land points (using an "if" statement, for instance), but it will not help in parallelization as the processor load is proportional to the number of grid points.

This paper presents global transport on a spherical multiple-cell (SMC) grid adapted from the Cartesian multiple-cell grid of Li (2003). The SMC grid relaxes the CFL restriction at high latitudes in a fashion similar to that of the reduced grid (Rasch 1994). Polar cells are introduced to remove the polar singularity of the differential transport equation by switching to an integral equation. The SMC grid is an unstructured grid, but finite-difference algorithms on a regular latitude–longitude grid can be used directly on the SMC grid. Upstream nonoscillatory (UNO) advection schemes (Li 2008) are implemented on the SMC grid and tested with solid-body rotation and deformation flows. Comparisons with results from previous studies and on different grids are attempted in these tests. Application of the SMC grid in an ocean surface wave model is also included to demonstrate its unstructured feature by removing all land points. A remedy for the invalid scalar assumption of the wave spectral bins at high latitudes is provided that enables global wave models to be extended into the entire Arctic Ocean.

2. Advection on SMC grid

In 2D spherical coordinates with latitude φ and longitude λ, the mass conservation equation, also called the continuity equation, is given by

$$\frac{\partial \psi}{\partial t} + \frac{\partial (u\psi)}{\partial x} + \frac{\partial (\upsilon\psi \cos\varphi)}{\cos\varphi\, \partial y} = 0, \qquad (1)$$

where ψ is the concentration of the transported quantity, t is the time, u and υ are the zonal and meridional velocity components, x and y are the local coordinates (x eastward along the parallel, y northward along the meridian), and $dx = r\cos\varphi\, d\lambda$, $dy = r\, d\varphi$, where r is the radius of the sphere. Since the length dimension is canceled out in the final transport scheme on the sphere, the radius can be set to any convenient value. For nondivergent flows, Eq. (1) is equivalent to the advection equation. For divergent flows, it differs from the advection equation by a divergence term. As velocity fields used for advection tests are always assumed to be nondivergent, Eq. (1) is frequently referred to as the advection equation. Also, note that Eq. (1) is equivalent to the Cartesian mass conservation equation except that the meridional differential term involves an extra cosine factor, which renders the term undefined (singular) at the poles. Thus, except for at the poles, the spherical continuity equation can be approximated using finite-difference schemes similar to ones used for the Cartesian continuity equation. The only difference between the Cartesian and spherical versions of these finite-difference schemes is that the latter has an extra cosine factor.

Because the polar singularity is not a physical singularity but rather is an artifact of the use of the spherical coordinate system, it can be removed if the differential Eq. (1) is replaced by its integral counterpart at the pole. Here, this is achieved by first introducing a *round polar cell* centered at the pole. Imagine the polar cell as a round coin of unit thickness, and assume that there is no flux crossing its top and bottom faces. Integrating Eq. (1) over this polar cell yields

$$\frac{\partial}{\partial t}\iint_{A_P} \psi\, dA = -\oint_{C_A} \psi \mathbf{v} \cdot d\mathbf{s}, \qquad (2)$$

where A_P and C_A are the area and circumference of the polar cell, respectively. The vector $d\mathbf{s}$ has a magnitude equal to the side-length increment and a direction that is outward and normal to the cell side. Assuming the polar cell is surrounded by m cells in a discrete model, Eq. (2) can be approximated as

$$\psi_P^{n+1} - \psi_P^n = \pm\frac{\Delta t}{A_P}\sum_{i=1}^{m} \psi_i^* \upsilon_i \Delta s_i, \qquad (3)$$

where the superscript n is the time-step index, Δt is the time step, ψ_i^* is the interpolated midflux value [see Li (2008) for its definition], υ_i is the meridional velocity, and Δs_i is the side length for the ith cell side that borders the polar cell. The sign in front of the r.h.s. of Eq. (3) is chosen to be positive for the North Pole and negative for the South Pole. Since finite-differencing assumes that any flux entering one cell becomes uniform within the cell in one time step, the polar cell will ensure instant cross-pole transport regardless of the face through which the flux enters the cell. So the polar cells have simultaneously removed the polar singularity in the continuity equation and achieved full cross-pole transport. Equation (3) is, in fact, a finite-volume formula, but it is broken down into individual fluxes in calculation with an equivalent finite-difference code. For this reason, it is called a finite-difference scheme.

This round polar cell approach is simpler than using triangular cells in a reduced grid for cross-pole transport. The fluxes entering the polar cells are calculated with the same formulation as off-pole cell fluxes because each polar cell is considered to be aligned along meridians with its surrounding cells, and there is no need to specify the velocity components at the poles for scalar transport. If the polar cells are required to hold vector variables such as the fluid velocity or the more complicated 2D wave energy spectrum used in ocean surface wave models, the directional vagueness at the poles has to be removed. One approach for 2D wave spectral transport across the Arctic will be discussed later.

The SMC grid is constructed in a similar way as the reduced grid (Rasch 1994), that is, by zonally merging cells above midlatitudes. The conventional latitude–longitude grid is built with trapezium-shaped cells, which share a constant meridional size $\Delta y = r\Delta\varphi$ but have a zonal size $\Delta x = r\Delta\lambda\cos\varphi$ that varies with latitude. The SMC grid is generated by zonally merging two cells into one above the latitude where Δx becomes less than half of the equatorial value $\Delta x_0 = r\Delta\lambda$. Thus, $\cos\varphi_1 = ½$ or, equivalently, $\varphi_1 = 60°$. Each merged cell above $\varphi_1 = 60°$ latitude has a reduced zonal resolution of $2\Delta\lambda$ (size 2). Farther north, where the size-2 cell length $2\Delta x$ is less than half of Δx_0, the cells are zonally merged again to $4\Delta\lambda$ (size 4), that is, above $\varphi_2 = \arccos(1/4) \sim 75.5°$. Generally, the kth size-changing parallel from size 2^{k-1} to size 2^k is located at $\varphi_k = \arccos(½^k)$ above the equator. For instance, the third size-changing parallel from size 4 to size 8 is at $\varphi_3 \sim 82.8°$, and the fourth from size 8 to size 16 is at $\varphi_4 \sim 86.4°$. For a discrete model grid, each size-changing parallel is rounded to the immediate grid parallel above it.

Figure 1 illustrates the global SMC grid at $\Delta\varphi = 1°$ and $\Delta\lambda = 1.125°$ resolution, which will be referred to as the SMC 1° grid. The stereographic projection is from (45°N, 60°W) so that both the polar and equatorial regions are visible. Between $-60°$ and 60°, there are 121 rows with 320 size-1 cells in each row ($N_1 = 121 \times 320$). The size-2 cells range from 61° to 76° in the Northern Hemisphere (16 rows), resulting in a total of $N_2 = 32 \times 160$ size-2 cells (including the Southern Hemisphere). Notice that the cell centers are at integer latitudes, so the first size-changing parallel is on the cell face at 60.5°, and the second size-changing parallel is at 76.5°. The size-4 cells range from 77° to 83°, or a total of $N_4 = 14 \times 80$ cells. Farther north are three rows of size-8 cells ($N_8 = 6 \times 40$) and two rows of size-16 cells ($N_{16} = 4 \times 20$), delimited by the third size-changing parallel at 83.5°, the fourth at 86.5°, and the fifth at 88.5°. The last size-changing parallel at 89.5° defines the polar cell, which is a round cell of diameter equal to Δy centered at the pole and surrounded by 10 size-32 cells ($N_{32} = 2 \times 10$). Note that the polar cells no longer obey the simple doubling rule, as the zonal size decreases more than twice within one latitude increment near the poles. In fact, each polar cell merges 10 size-32 cells. The polar cell area ($0.25\pi\Delta y^2$) is on the same order as the areas of other cells ($\xi\Delta y^2$, where ξ varies from 0.5625 to 1.125). The total number of cells in the SMC 1° grid is 45 302, about 79% of that on the latitude–longitude grid (180 × 320).

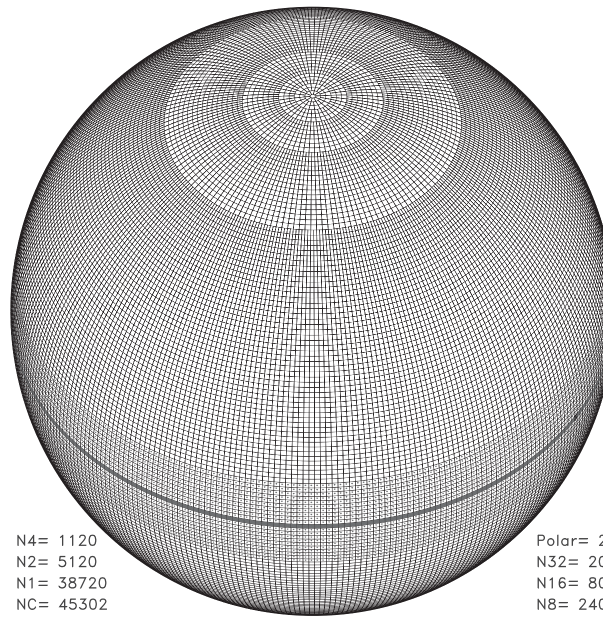

FIG. 1. The SMC 1° grid. There are 180 cells along a meridian and 320 cells along the equator. The cells are zonally merged in several steps toward the poles, ending at each pole with a round polar cell. Total number of cells is 45 302, about 79% of the standard grid (180 × 320 cells). Cells centered on the equator are filled gray. The dotted cells indicate the equatorial stripe of the initial spherical step function used in the solid-body rotation test and the small letter s on the equator marks the rotational south pole.

The apparent difference between the SMC grid and the reduced grid (Rasch 1994) is the introduction of the round polar cell in the SMC grid. The use of triangular cells around the pole in the reduced grid could cause partial ''blocking'' if the meridional fluxes at the pole are suspended. The major difference between the SMC grid and the reduced grid is the unstructured cell arrangement of the SMC grid. Using the multiple-cell grid technique (Li 2003), the cells can be listed in any order, with the freedom to add or to remove any cells as necessary. A cell (index) array is created to hold information on the position and size of each cell in a given cell list. The cell array is used to map a cell's value onto the conventional latitude–longitude grid or vice versa. It is also used to guide cell-list-oriented loops. The rectangular (or trapezoidal if the spherical curvature is taken into account) cell shape is one major advantage of the SMC grid over other unstructured grids such as the hexagon cells used by the spherical geodesic grid (Lipscomb and Ringler 2005) and the triangular cells used by finite-element grids (Hanert et al. 2004). The rectangular cell shape allows finite-difference schemes to be applied directly to the SMC grid using the same stencil as on the conventional latitude–longitude grid. It also allows for a straightforward mapping onto the conventional latitude–longitude grid. This straightforward mapping between the two grids allows the two grids to be used together in one model. For instance, in a climate model, the chemical tracers may be transported on the SMC grid while its wind field is solved by a dynamical core on the standard latitude–longitude grid.

In this study, two UNO advection schemes of second- (UNO2) and third- (UNO3) order accuracy (Li 2008) are implemented on the SMC grid. They are derived by combining existing advection schemes in different monotonic regions. UNO2 is an extension of the MINMOD scheme (Roe 1985). In the UNO2, the interpolated value at the midflux point for a given cell face is given by

$$\psi^{\mathrm{MF}}_{j+1/2} = \psi_C + 0.5\ \mathrm{sgn}(\psi_D - \psi_C)(\Delta x_C - |u_{j+1/2}|\Delta t) \times \min(|G_{\mathrm{DC}}|, |G_{\mathrm{CU}}|), \qquad (4)$$

where $j + ½$ is the cell face index; the subscripts U, C, and D indicate the upstream, central, and downstream cells, respectively, relative to the given $j + ½$ cell face velocity $u_{j+1/2}$; Δx_C is the grid length of the central cell; and G_{DC} (or G_{CU}) is the gradient of the transported field between the D and C (or C and U) cells [i.e., $G_{\mathrm{AB}} \equiv (\psi_A - \psi_B)/(x_A - x_B)$]. UNO3 follows the ULTIMATE QUICKEST scheme (Leonard 1991) in using a third-order scheme (Takacs 1985) as its central part but replaces the flux limiters in ULTIMATE QUICKEST with a doubled MINMOD scheme. UNO3 switches to UNO2 outside the monotonic region. An advective-conservative hybrid operator (Leonard et al. 1996) that reduces the time-splitting error is used to extend the UNO schemes to multidimensions. Details of the UNO schemes are given in Li (2008) alongside standard numerical tests, which demonstrate that the UNO schemes on Cartesian multiple-cell grids are nonoscillatory, conservative, shape preserving, and faster than their classical counterparts.

As the UNO schemes are given in upstream-center-downstream (UCD) notation, their implementation on the SMC grid requires information from two cells on each side of a given cell face for evaluation of the face flux. The neighboring cell information can be preprocessed with the aid of the cell array and stored in a face array, which serves as a set of pointers to link the face flux to its UCD cells. The advection flux is then evaluated in a loop controlled by the face array. Cell-face widths are included in the flux evaluation to accommodate the variations in cell size with latitude.

No interpolation for meridian alignment is required on the SMC grid even for fluxes across size-changing parallels. Each merged cell is considered to be two identical subcells of the premerging size, and its value is used directly in the flux calculation as if its cell center is still aligned along the meridian with the cells on the other side of the size-changing parallel. This is also true for the calculation of fluxes into (or out of) the polar cells as each polar cell is aligned along meridians with its surrounding cells. A temporary variable is used to hold all fluxes (or net flux) into a given cell before all flux evaluations are completed. Cell values are updated in a separate cell loop with the net flux variables. As a result, the two fluxes into the same merged cell above a size-changing parallel are automatically added up when the cell value is updated. This also makes the update of each polar cell blend in smoothly with the updates of off-pole cells except for its unique cell area and the net sum of v fluxes given in Eq. (3). So the finite-volume fluxes entering the polar cells or crossing the size-changing parallels have been converted into equivalent finite-difference codes.

The zonal cyclic boundary conditions used in the global latitude–longitude grid are naturally incorporated into the face array. The southern and northern boundaries disappear in the SMC grid because they have been incorporated into the polar cells. So the global transport of a scalar variable on the full global SMC grid does not need any boundary conditions. This is an advantage for optimization.

3. Solid-body rotation tests

A solid-body rotation velocity field is used to demonstrate advection on the SMC 1° grid. Assuming the rotational pole is at longitude λ_P and latitude φ_P and the constant angular speed is ω, the zonal and meridional velocity components (u and v) of this solid-body rotation flow are given by

$$u = \omega r[\cos\alpha \cos\varphi - \sin\alpha \sin\varphi \cos(\lambda - \lambda_P)],$$
$$v = \omega r \sin\alpha \sin(\lambda - \lambda_P), \quad \alpha \equiv \pi/2 - \varphi_P. \qquad (5)$$

The angular velocity ω is set to $10°\ \mathrm{h}^{-1}$, equivalent to a rotation period of 36 h. The time step is set to 150 s and

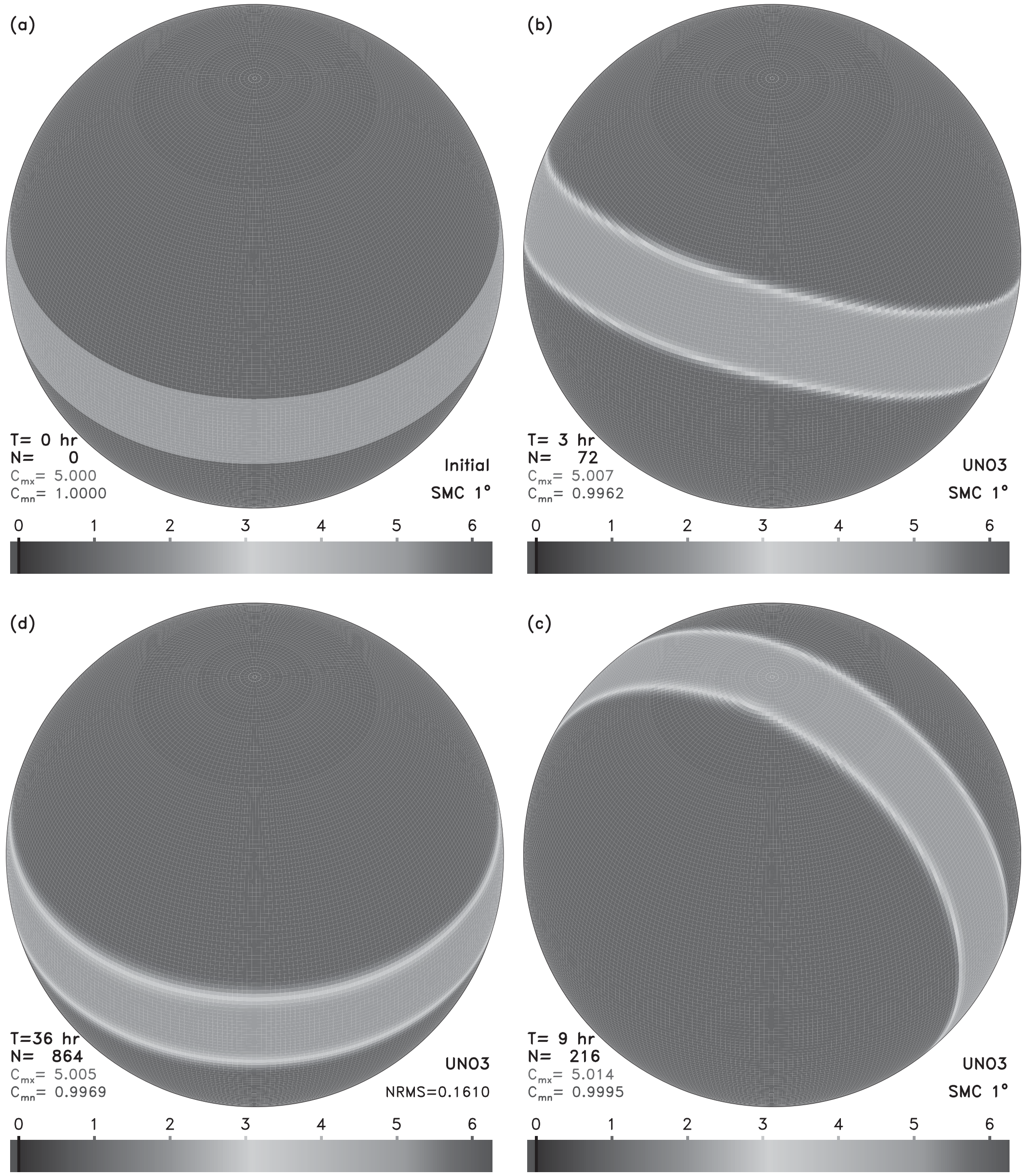

FIG. 2. Solid-body rotation of an SSF using the UNO3 scheme on the SMC 1° grid. The same viewpoint as in Fig. 1 is used in all panels. The rotational pole is on the equator and the rotation angular speed is 10° h^{-1}.

the maximum Courant number is about 0.754. A full cycle around the sphere then takes 864 time steps.

The initial condition is a spherical step function (SSF), which is constructed by setting all cell values to 1.0 unit except for cells within a 20°-wide stripe along the equator. Cells within this stripe are initially set to 5 units and are marked by dots in Fig. 1. The rotational pole is chosen on the equator ($\varphi_P = 0$ or $\alpha = \pi/2$) at $\lambda_P = \pi$, and the small letter s in Fig. 1 marks the rotational south pole. The initial SSF field is shown in Fig. 2a ($t = 0$ h) with exactly the same stereographic projection as in Fig. 1. The SSF range is indicated by the maximum ($C_{\rm mx} = 5.0$) and minimum ($C_{\rm mn} = 1.0$) cell values printed in the panel's lower-left corner. The color keys have 40 levels per unit (total 256 levels) or a resolution of 0.025 units. Each cell value is displayed by rounding it to the nearest color level. Because the initial SSF consists of only two values (the 1-unit background and the 5-unit stripe), it is displayed in two colors in Fig. 2a. The SSF is used as part of the initial conditions because its sharp edges are very sensitive to numerical oscillations. In this spherical solid-body rotation test, the circular stripe sweeps over the full sphere. Thus, any oscillations generated by the UNO schemes and/or the presence of the size-changing parallels will become immediately apparent.

Figure 2b shows the solid-body rotation result with the UNO3 scheme after $t = 3$ h or 30° rotation. The obvious differences from the initial conditions (Fig. 2a) are the rounded edges of the stripe. The initial sharp edges have been smoothed by the numerical diffusion, resulting in a continuous transition zone from the stripe top (5 units) to the background (1 unit). This transition zone is illustrated by the intermediate colors between 1 and 5. Note that the maximum and minimum values are now 5.007 and 0.9962 units, indicating a very small oscillation generated by the UNO3 scheme on the SMC grid. This is likely the result of the distortion of the cell shapes from rectangular due to the spherical curvature. In fact, close examination reveals that the oscillations are associated with the stripe edges and reach a local maximum when the edges are rotated to high latitudes. This can be further illustrated by the $t = 9$ h result (Fig. 2c) when the initial stripe has been rotated 90° to cover the poles. The maximum value is 5.014 units at this time, the largest value in the whole test. The polar cells are in the middle of the stripe after the 90° rotation, and their values are very close to those of the 20 cells surrounding them. This indicates that the SSF passes through the size-changing parallels and the polar cells smoothly.

Figure 2d shows the solid-body rotation result after one full cycle at $t = 36$ h or $N = 864$ steps. The maximum and minimum values (5.005 and 0.9969) indicate that the small oscillation at the stripe edges persists but is smaller than when the stripe crosses the pole (Fig. 2c). By this time, the stripe has returned back to its initial position, and it is apparently identical to the initial conditions (Fig. 2a) except for its rounded edges. Direct comparison of this result with the initial SSF can reveal the quality of the UNO3 advection on the SMC grid. Following Williamson et al. (1992), a normalized root-mean-square (NRMS) error is defined as

$$\mathrm{NRMS} = \left[\sum(\psi_i^n - \psi_i^{\mathrm{ref}})^2 A_i \Big/ \sum(\psi_i^{\mathrm{ref}})^2 A_i\right]^{1/2}, \qquad (6)$$

where the summation is over all cells, A_i is the area of the ith cell, and ψ^{ref} is a reference field. For this SSF rotation test, the reference field is simply chosen to be the initial SSF or ψ^0. The SSF one-cycle NRMS error on the SMC 1° grid with the UNO3 scheme is 0.1610 (Fig. 2d).

Using the UNO2 scheme on the SMC 1° grid for rotation of the same SSF shows a very similar result except that the smoothing is slightly stronger than for the UNO3 scheme. Table 1 compares the NRMS errors generated by the UNO2 and UNO3 schemes on the SMC 1° grid for up to 3 cycles and their total CPU times. The SSF 1-cycle NRMS error for UNO2 is 0.2127, larger than that for UNO3 (0.1610). Both schemes have their largest error increments in the first cycle and slightly increased ones in the subsequent 2 cycles. The slowing down of the smoothing by the advection scheme is described as self-limiting (Allen et al. 1991) because the implicit numerical diffusion is less effective on a smoothed field than on the initial step discontinuity. In fact, the NRMS for the UNO3 scheme remains as little as 0.1763 and 0.1857 for the last 2 cycles (Table 1), corresponding to about a 10% and a 5% increase, respectively. The NRMS for the UNO2 scheme increases by about 15% and 5% for the last two cycles. The CPU times listed in Table 1 are for 3 cycles (2592 time steps) on a desktop machine (Dell Precision T3500) without any output writing. So they reveal the net calculation time using the two schemes, respectively. The UNO2 scheme is about 30% faster than UNO3. Considering this 30% CPU time reduction, the small loss of accuracy by UNO2 is worthwhile, especially if smoothing is required, as for example the horizontal diffusion in ocean models (Killworth et al. 2003) and the smoothing term in ocean wave models (Tolman et al. 2002).

TABLE 1. NRMS errors and CPU time for the solid-body rotation test of the SSF using the UNO2 and UNO3 schemes on the SMC 1° grid. Errors are given after each of 3 full cycles. CPU time is for 3 full cycles. Maximum Courant number is 0.754.

	$N = 864$	$N = 1728$	$N = 2592$	CPU time (s)
UNO2	0.21267	0.24429	0.26980	6.212
UNO3	0.16096	0.17625	0.18574	8.847

The SSF rotation test is also used to compare transport on the SMC grid with transport on the standard latitude–longitude and reduced grids. The standard latitude–longitude 1° grid has 180 × 320 (=57 600) cells with 320 triangular cells around each pole. The reduced 1° grid is identical to the standard 1° grid below 60° latitude and, like the SMC grid, merges cells zonally toward the poles except for the last row of cells around each pole. The reduced 1° grid uses 5 triangular cells around each pole and has 44 990 cells in total. For comparison purposes, a new SMC grid is used and is made identical to the reduced 1° grid except that it merges the five triangular cells into a single round polar cell at each pole. Thus, its total cell number (44 982) is 8 cells less than that of the reduced 1° grid. Note that this new SMC grid differs slightly from the SMC 1° grid shown in Fig. 1 and will be referred to as the SMC 1° b grid. Each polar cell on the SMC 1° grid occupies only a half row. This half-row shift makes each polar cell approximately as large as its surrounding cells in area. Each polar cell on the SMC

TABLE 2. Comparison of the standard latitude–longitude, reduced, and SMC 1° grids for the SSF rotation tests with UNO3.

	No. cells in total	Time step (s)	Max Courant No.	NTS per cycle	CPU time per cycle (s)	CPU time per step (ms)	NRMS after one cycle
Standard	57 600	3	0.849	43 200	228.158	5.281	0.169 05
Reduced	44 990	150	0.716	864	3.215	3.721	0.164 43
SMC1°b	44 982	150	0.716	864	3.169	3.668	0.164 57

1° b grid, however, is 4 times as large as the SMC 1° grid polar cell. The SMC 1° b grid shares exactly the same grid mesh as the reduced and the standard 1° grids below 60° latitude so that exactly the same initial SSF stripe can be used on all three grids. The rotation speed is kept at 10° h^{-1}, and the UNO3 scheme is used with all three grids.

Results from the SSF rotation tests on the three grids are listed in Table 2. Due to the CFL restriction, the time step for the standard 1° grid has to be reduced to 3 s, leading to a maximum Courant number of 0.849. The number of time steps (NTS) required to complete one cycle is increased to 43 200. A 2D-structured regular grid code is used for the SSF rotation on the standard 1° grid. The structured code is verified by checking its output every hour for 3 cycles. Then, all output is suppressed for a one-cycle (43 200 step) CPU timing run. This takes 228 s on a desktop machine (Dell Precision T3500) and generates a one-cycle NRMS error of 0.169 05. This corresponds to an average CPU time of 5.28 ms per time step. The unstructured irregular-grid SMC code can be applied on the standard grid by setting all cells to be size 1. But it costs 289 s of CPU time, 26% more than the regular grid version, due to the extra size factors and grid-length divisions in the flux calculations.

The time step for the reduced 1° grid and the SMC 1° b grid is set to 150 s, the same as that for the SMC 1° grid (but 50 times longer than for the standard 1° grid), leading to a maximum Courant number of 0.716 for the same rotation speed of 10° h^{-1}. It then takes only 864 steps to finish 1 cycle. With the reduced 1° grid, this requires only 3.215 s of CPU time. The 1-cycle rotation on the SMC 1° b grid takes 3.169 s, even less time than that for the reduced 1° grid. This is not a surprise because the reduced 1° grid has eight more cells than the SMC 1° b grid and uses the same unstructured SMC model code. The one-cycle NRMS error of the rotated SSF on the SMC 1° b grid is 0.164 57, slightly larger than that of the reduced 1° grid (0.164 43). Despite the reduced spatial resolution in the polar regions and the use of only a fraction (~1.4%) of the CPU time, the SSF 1-cycle NRMS errors on both the reduced 1° grid and the SMC 1° b grid are still smaller than that on the standard 1° grid (0.169 05). The average CPU time per step (3.721 ms for the reduced grid and 3.668 ms for the SMC grid) is also smaller than that for the standard grid (5.28 ms) because of the substantial reduction (~22%) in cell count. So both grids are significantly more efficient than the standard grid without sacrificing the accuracy of the scalar global transport.

Subtle differences among the three grids may be revealed by close examination of the SSF at 90° rotation in Fig. 3. The suppressing of meridional fluxes at the polar vertices of the triangular cells on both the standard and the reduced grids causes partial blocking of transport across the Pole. This blocking effect is visible in Fig. 3a, which shows the SSF field in the polar region at $t = 9$ h on the standard 1° grid. The blocking effect is revealed by the dent in the SSF field downstream of the North Pole. Some cell values (every 16th) from the top three rows are presented in Fig. 3a to aid in the analysis. The zonal index i runs from 0 to 319, and cells with $i = 80$ are located directly downstream of the North Pole. The $i = 80$ cell values on the three rows immediately south of the North Pole (4.997, 4.996, and 4.992) are smaller than other cell values along these three rows.

The blocking effect is less obvious on the reduced 1° grid (Fig. 3b) than on the standard 1° grid due to the former's reduced resolution and hence increased implicit diffusion. However, it is still evident in the printed cell values. The second triangular cell (corresponding to $i = 64$–127 on the standard grid) has the smallest value (4.911) among the five triangular cells on the top row. The downstream cell values on the other two rows behave in a more ambiguous way, most likely because the diffusion and oscillation have muffled the signal. This implies that the blocking effect is of the same order as the numerical diffusion.

The SMC 1° b grid results (Fig. 3c) have removed the blocking. In fact, the third cell (corresponding to $i = 64$ to 95 on the standard grid) of the 10 cells surrounding the polar cell contains the maximum value (5.013) on the full field. The third-row values behave ambiguously as in the reduced grid case, although the field is smoother than that of the reduced grid. However, the gain in accuracy achieved on the SMC 1° b grid by replacing the five triangular cells with the polar cell is almost canceled out by the extra diffusion error due to the increased size of the polar cell. If the polar cells are of a size similar to other cells as on the SMC 1° grid, the NRMS error decreases to 0.160 96 (see Fig. 2d), smaller than for any of

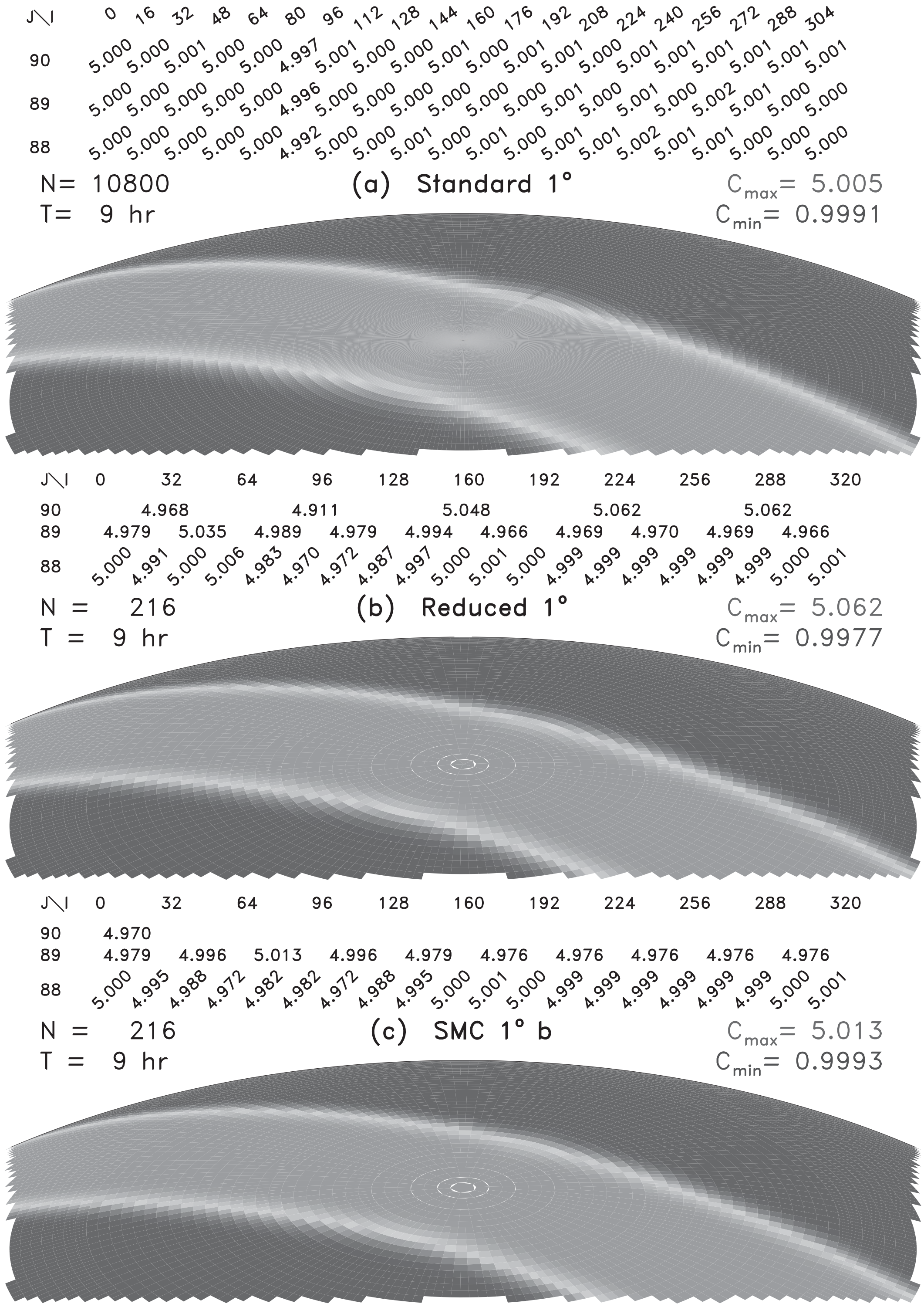

FIG. 3. (a)–(c) Comparison of the standard latitude–longitude, reduced, and SMC 1° b grids after 90° rotation of the SSF with the UNO3 scheme.

the three grids (see Table 2). Note that the white gaps at size-changing parallels in Figs. 3b and 3c are plotting artifacts (not the solution) due to projecting cells as quadrilaterals, except for the polar cell in Fig. 3c, which is mapped as a pentagon.

4. Classical spherical transport tests

A double-vortex deformation test and a cosine bell solid-body rotation test are used here for comparison with other spherical grid and advection scheme combinations.

a. Deformation test

The nondivergent spherical deformation flow with two symmetric vortices around rotated poles is adapted from Nair and Machenhauer (2002). It is defined by the angular speed ω as a function of the rotated latitude, φ', relative to its rotational pole as follows:

$$\omega(\varphi') = \omega_0 \frac{\sinh\beta}{\beta\cosh^3\beta}, \quad \beta \equiv 3\cos\varphi'. \tag{7}$$

Here, ω_0 is the maximum angular speed when β becomes 0 or at the rotational poles. To avoid division by zero in the computer code, ω is set to ω_0 if $\beta = 0$. The angular speed ω has a minimum value of about $0.0085\omega_0$ on the rotated equator ($\varphi' = 0$). The deformation flow is similar to the solid-body rotational flow except that the angular speed varies with the rotated latitude. Note that the simplified angular speed definition Eq. (7) is independent of the sphere radius and is equivalent to the original definition [combined Eqs. (35) and (36) in Nair and Machenhauer (2002)]. The rotation speed peaks at $\varphi' = \pm\cos^{-1}[\sinh^{-1}(\sqrt{2}/2)/3] \sim \pm77.32°$, or about 13° from the rotational poles.

For a given initial distribution $\psi_0(\lambda', \varphi')$ as a function of the rotated coordinates, the exact solution at time t generated by this deformation field is given by $\psi_0(\lambda' - \omega t, \varphi')$. The following analytical solution has been recommended by Nair and Machenhauer (2002):

$$\psi(\lambda', \varphi', t) = 1 - \tanh[0.6\cos\varphi' \sin(\lambda' - \omega t)]. \tag{8}$$

The rotational pole is usually set apart from the grid pole by using a rotated coordinate system. The deformation velocity field [Eq. (7)] and the exact solution [Eq. (8)] can be expressed in terms of λ and φ using the mapping from the rotated to the original coordinate systems. Details of this mapping are available in Ritchie (1987) or Nair et al. (1999). For comparison purposes, this test will use the recommended angular speed parameter $\omega_0 = 1.5\sqrt{3}$ and the rotational north pole at $(\lambda_P, \varphi_P) = (\pi + 0.025, \pi/2.2)$.

One difficulty in comparing results on the SMC grid to previous studies that use the standard 64 × 128 latitude–longitude grid (Nair and Machenhauer 2002; Zerroukat et al. 2004) is the difference between the two grids in the spatial distribution of the grid resolution. The standard latitude–longitude grid has a much higher resolution in the polar region than near the equator, while the SMC grid has a balanced spatial resolution over the globe. Thus, the polar resolution of the SMC grid would be too coarse if it were to use the same equatorial resolution as the standard 64 × 128 grid. Here, the comparison will be based on grids with similar average resolution. For this purpose, an SMC 2° grid is constructed by doubling the grid length of the SMC 1° grid so that its total cell count is close to that of the standard grid. The effects of spatial resolution in the SMC grid can be studied by comparing the two SMC grids. The SMC 2° grid is shown in Fig. 4b. It has 160 cells along the equator ($\Delta\lambda = 2.25°$) and 90 cells along a meridian stretching from the South to the North Pole ($\Delta\varphi = 2°$). The SMC 2° grid merges cells zonally in a similar way as the SMC 1° grid and also ends with 10 cells around each polar cell. The cell count of the SMC 2° grid is 11 142, about a quarter of the SMC 1° grid (45 302). The cell count of the standard 64 × 128 grid is 8192, roughly 74% of that of the SMC 2° grid.

Figure 4a shows the analytic solution at $t = 0$. This is also used as part of the initial conditions for the simulations. The range of the initial field is from 0.462 99 to 1.5370. All panels in Fig. 4 are viewed from (75.0°N, 1.5°E) in order to clearly show the polar vortex. The rotational north pole at (81.818°N, 178.57°W) is indicated by the letter N. For the SMC 2° grid, the time step is set to 0.04, and the maximum Courant number is 0.606. The analytic solution at $t = 6$ is shown in Fig. 4c, and the simulated one with the UNO3 scheme on the SMC 2° grid is shown in Fig. 4d. The two fields are in good agreement, and this is confirmed by the small NRMS error (0.012 14), evaluated with Eq. (6). This indicates that the UNO3 scheme on the SMC grid performs well for scalar transport in this deformation flow. The transport across the size-changing parallels (including the polar cells) is smooth, as there are no visible oscillations along these parallels.

Figures 4e and 4f show the analytic and simulated solutions to the deformation flow at $t = 6$ with UNO3 on the SMC 1° grid. In this case, the time step is set to 0.02, and the maximum Courant number is 0.676. The increased spatial resolution has led to improved accuracy, as is evident by the reduced NRMS error (0.003 45). With time, the analytic solution develops an increasingly finescale spiral structure that eventually passes beyond the resolution of any discrete grid. The finescale structure will be smoothed out by the implicit diffusion of the advection scheme, resulting in a simulated solution

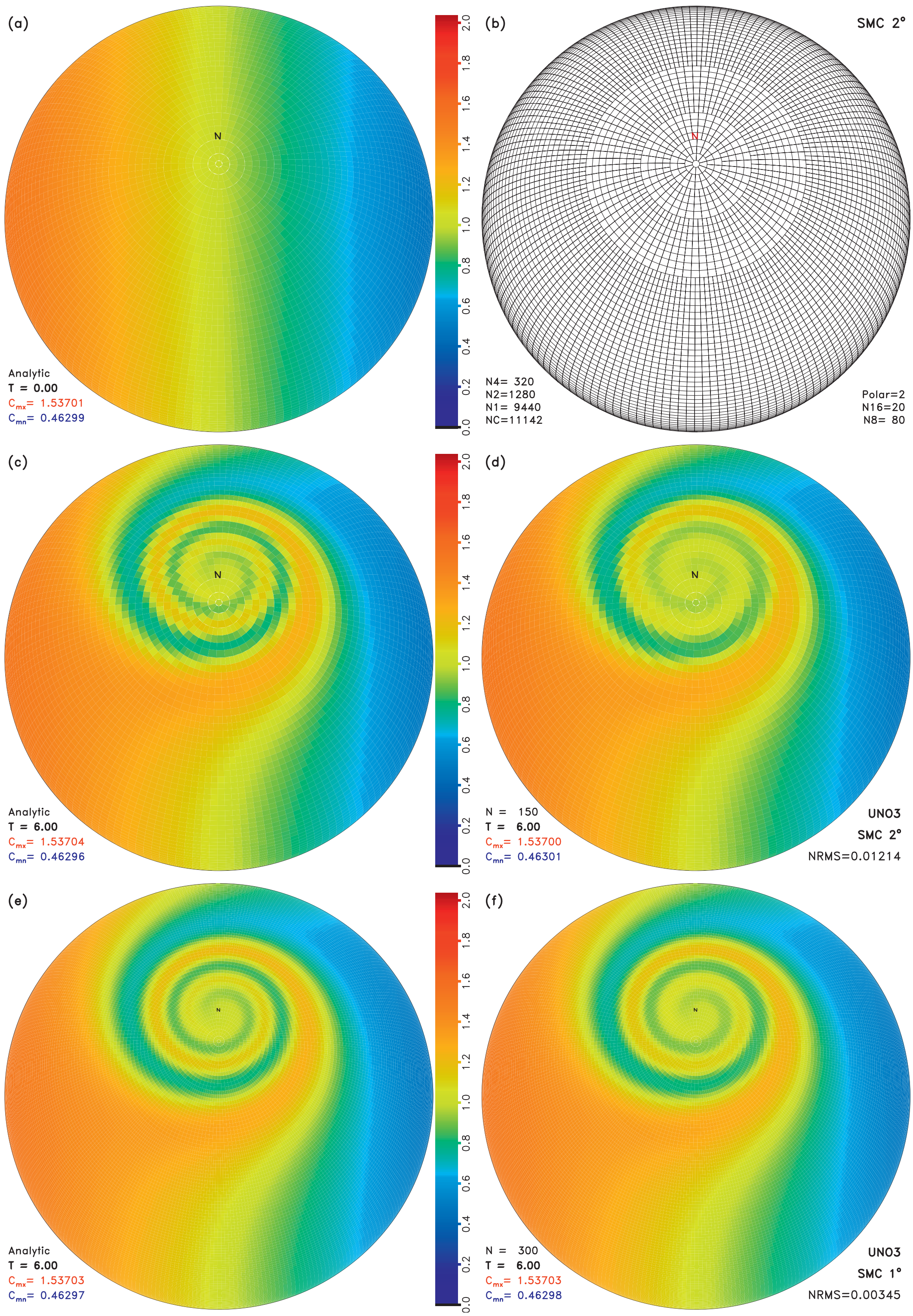

FIG. 4. (left) Analytic and (right) simulated solutions to the spherical deformation flow at t = 6 with the UNO3 scheme on the (c),(d) SMC 2° and (e),(f) SMC 1° grids. (a) The initial conditions and (b) the SMC 2° grid. Note that the rotational north pole (denoted by N) is offset from the grid North Pole by about 8.2°.

TABLE 3. NRMS errors for the spherical deformation flow using the UNO2 and UNO3 schemes on the SMC 1° and 2° grids. NRMS errors by other authors (NM02 and ZWS04) are also listed here but only as an approximate guide; the tests are not directly comparable due to differences in grid resolutions and between the Eulerian and semi-Lagrangian schemes.

	$T = 3$	$T = 6$	$T = 9$	$T = 12$
SMC 1° UNO2/UNO3	0.001 64/0.000 79	0.009 26/0.003 45	0.021 23/0.012 13	0.029 74/0.021 93
SMC 2° UNO2/UNO3	0.004 40/0.002 23	0.018 88/0.012 14	0.030 88/0.025 05	0.039 14/0.033 37
SLICE-S (ZWS04)	0.002 56	0.011 47		
BiCubic-SL (ZWS04)	0.001 83	0.014 23		
CISL-N/P (NM02)	0.0025			

equivalent to the grid average of the analytic solution. This kind of smoothing of the fine vortex structure is not unique to the UNO3 scheme but is a limitation common to all finite-difference schemes.

Using the UNO2 scheme on the SMC grids for this deformation flow produces results that are very similar to the ones using UNO3, the only difference being slightly enhanced smoothing of the UNO2 solution. Table 3 lists the NRMS errors with these two schemes. The NRMS error with the UNO2 scheme on the SMC 1° grid at $t = 3$ is 0.001 64, about twice that of the UNO3 value (0.000 79). The NRMS error ratio of the two schemes is about the same on the SMC 2° grid, though both errors increase as resolution is decreased. The difference between the two schemes becomes smaller with time because both solutions eventually approach the same uniform field.

Also listed in Table 3 are some published results on the standard 64 × 128 latitude–longitude grid using SL schemes. These are the Semi-Lagrangian Inherently Conserving and Efficient scheme for transport on a Sphere (SLICE-S) and BiCubic-SL schemes of Zerroukat et al. (2004, hereafter ZWS04) and the mass-conservative Cell-Integrated Semi-Lagrangian scheme without any filter (CISL-N) of Nair and Machenhauer (2002, hereafter NM02). The UNO3 scheme on the SMC 2° grid can match the SL schemes in this test and can produce a more accurate result on the SMC 1° grid. In fact, the UNO2 scheme on the SMC 1° grid also outperforms the SL schemes on the standard 64 × 128 grid. It should be emphasized that the average spatial resolution of the SMC 2° grid is slightly higher than that of the standard 64 × 128 grid, so the results are not fully comparable. They should not be interpreted as a claim that the UNO3 scheme is more accurate than the SL schemes. On the contrary, these SL schemes are more accurate than the UNO3 scheme, as will be demonstrated in the cosine bell test below. The advantage of using the UNO scheme on the SMC grid is its simplicity.

b. *Cosine bell rotation*

The solid-body rotation of a cosine bell recommended by Williamson et al. (1992) is widely used by modelers for global transport scheme assessments. The cosine bell definition is rewritten to be independent of the sphere radius as

$$\psi(\lambda, \varphi) = h_0[1 + \cos(3\pi\gamma)], \quad \text{if} \quad \gamma < 1/3$$
$$\cos\gamma = \sin\varphi_C \sin\varphi + \cos\varphi_C \cos\varphi \cos(\lambda - \lambda_C), \qquad (9)$$

where h_0 is half the bell height and φ_C and λ_C are the latitude and longitude of the bell center, respectively. Outside the bell edges defined by $\gamma = 1/3$, the bell function $\psi(\lambda, \varphi)$ is set to 0. By tracing the bell center with time, Eq. (9) yields the exact solution to the rotated cosine bell at any given time. The three velocity fields recommended by Williamson et al. (1992) are given by Eq. (5) with the rotational pole at $\lambda_P = \pi$ and $\alpha = \pi/2$, $\pi/2$–0.05, and 0.0, respectively. The initial bell center is positioned on the equator at 90°W or $(\lambda_0, \varphi_0) = (3\pi/2, 0)$. The original recommended rotation period is 12 days, but 36 h is used here ($\omega = 10° \text{ h}^{-1}$). As time is a relative quantity in an advection test because it is canceled out by the time in the rotation speed during the evaluation of the Courant number, a large rotation speed can be compensated by a reduced time step. This will not affect the simulation results as long as the same Courant number is used. The time step is maximized for each test with the restrictions that 1 h is a multiple of the time step (for output at every hour) and the maximum Courant number is less than 0.9, which is used by Hubbard and Nikiforakis (2003, hereafter HN03). The maximum Courant number and time step for each test are listed in Table 4.

Figure 5a shows the exact cosine bells at three times (t = 5, 9, and 36 h) mapped onto the SMC 2° grid for the $\alpha = \pi/2$ case. Since the cosine bell returns to its initial

TABLE 4. Maximum Courant number Co_{max} and time step Δt (s) used in each cosine bell test on the SMC 1° or SMC 2° grid. The angular speed $\omega = \pi/18 \text{ h}^{-1}$ is fixed for all tests.

	$\alpha = \pi/2$	$\alpha = \pi/2$–0.05	$\alpha = 0$
SMC 1°Co_{max} (Δt)	0.754 (150)	0.758 (150)	0.889 (360)
SMC 2°Co_{max} (Δt)	0.789 (360)	0.794 (360)	0.889 (720)

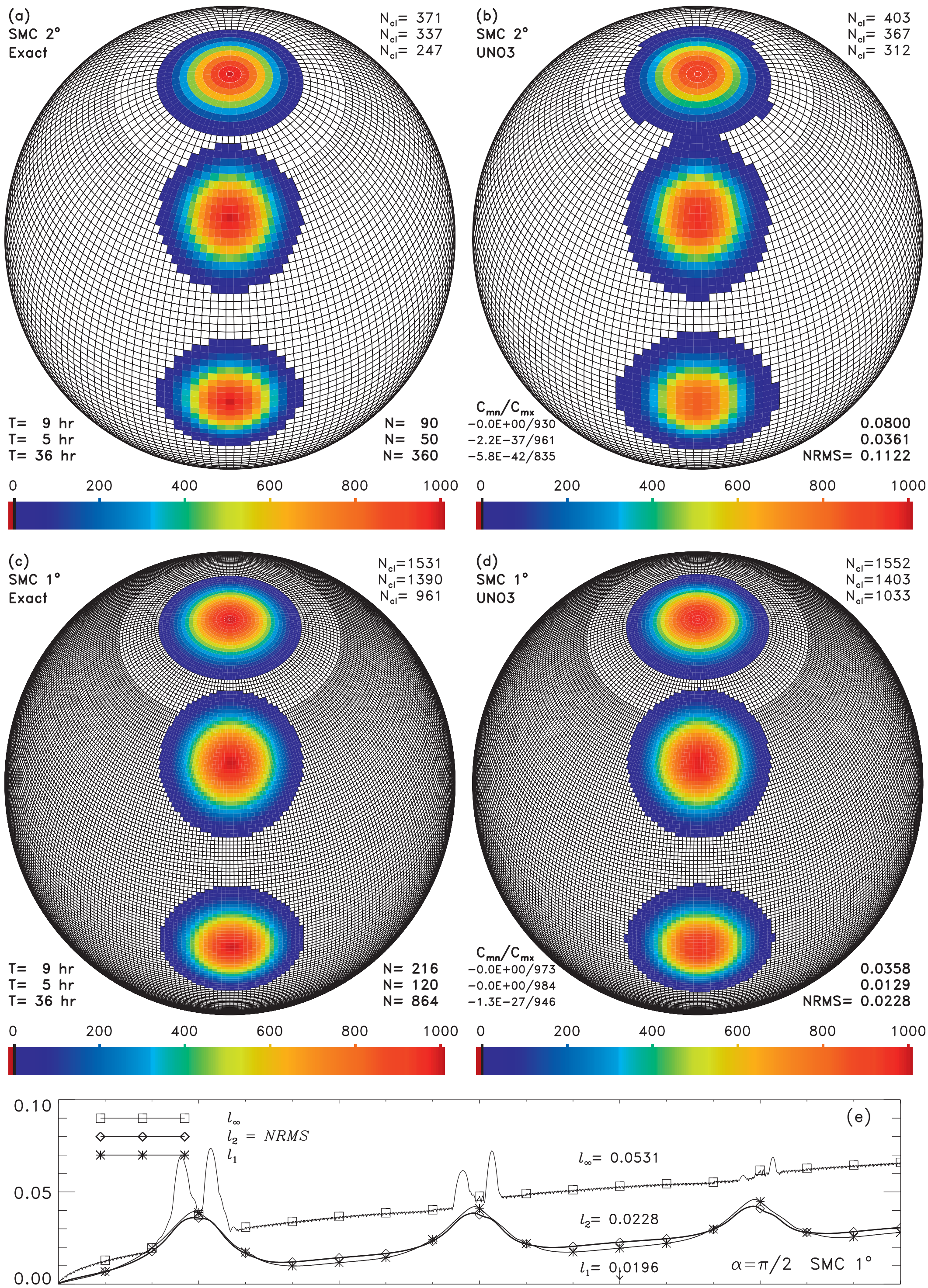

FIG. 5. (left) Exact and (right) simulated solid-body rotation ($\alpha = \pi/2$) of a cosine bell on the (top) SMC 2° and (middle) SMC 1° grids with the UNO3 scheme and (bottom) error norms.

location after a full cycle, the bell at $t = 36$ h is identical to the initial one (bottom bell in Fig. 5a). The bell height is scaled by the constant, h_0, which is canceled out in the NRMS expression Eq. (6). So the absolute value of h_0 does not affect the normalized errors. For comparison purposes, the value of $h_0 = 500$ units is chosen to be the same as in the standard test of Williamson et al. (1992). There are 250 color levels from the bell base (0) to its peak (1000 units) at 4-unit intervals. There are also 3 color levels below the 0 background and 2 levels above the maximum bell height to accommodate numerical oscillations, if any. Each cell value is rounded to the nearest color except for the 0 background (between ± 2 units). Cells with values in this 0-background range are not colored in, allowing the grid underneath to be seen. This is done to make it easier to pinpoint the location of the bell with time.

The number of colored cells (N_{cl}) within an angular radius of $\gamma = 1/3$ for each of the three exact bells is shown in the top-right corner of Fig. 5a. The initial bell (or $t =$ 36 h) has 247 colored cells. The cosine bell after a 50° rotation ($t = 5$ h) strides two cell-size zones and demonstrates the crossing of a size-changing parallel. Because of the decreasing zonal grid length, the bell covers more cells (337) here than at its initial position. After a 90° rotation ($t = 9$ h), the center of the bell arrives at the North Pole. The number of colored cells increases to 371, about 50% more than the initial value (247). This increase reflects the fact that, despite the cell merging at high latitudes, the resolution of the SMC grid is still higher in the polar region than on the equator. This is not a surprise because the actual size of any merged cell does not exceed that of one equatorial cell on the SMC grid.

Figure 5b shows the simulated cosine bells after 50°, 90°, and 360° rotations ($\alpha = \pi/2$) with the UNO3 scheme on the SMC 2° grid. Comparing these to the exact solutions on the left, it can be seen that the simulated bells are similar to the exact solutions except for their reduced peaks and enlarged bell edges due to the implicit numerical diffusion in the advection scheme. The minimum and maximum (bell peak) values of the simulated bell are listed in the bottom-left corner of Fig. 5b. The peak is reduced by about 17% ($C_{\mathrm{mx}} = 835$ unit) from the initial 1000 units after one cycle. There are also very small oscillations as the minimum values ($C_{\mathrm{mn}} < 10^{-36}$ unit) indicate. The NRMS errors for UNO3 on the SMC 2° grid are listed in the bottom-right corner of Fig. 5b. The full cycle NRMS for this case is 0.1122.

The enlarged area of the simulated bell is indicated by the total number of colored cells, as shown at the top-right corner of Fig. 5b. After a full rotation, the number of colored cells increases to 312, equal to a 26% increase from the initial value (247). The 50° rotation result (middle bell) shows that the transport across the size-changing parallel occurs smoothly. The 90° rotated cosine bell on the North Pole illustrates well the asymmetry of the numerical diffusion. The simulated bell has 32 extra colored cells along the front and rear edges, indicating that the numerical diffusion is stronger in the direction of the flow than in the cross-flow direction. This is in agreement with the implicit diffusivity analysis of Li (2008). In addition, the spatial resolution change also contributes to the asymmetry. The bell center is initially chosen to coincide with a size-1 cell on the equator so that the bell is symmetrical. As it is moved to high latitudes, the bell center no longer coincides with the merged cells except when it is at the pole. This also reveals the fact that the ''exact'' solution is not exactly the same at different positions due to the resolution change.

Figures 5c and 5d show the exact and simulated cosine bells for the same test ($\alpha = \pi/2$) with the UNO3 scheme but on the SMC 1° grid. The increased accuracy is obvious by visual comparison of the two panels and by the extreme (min and max) and NRMS values. The 90° rotated bell is nearly as round as the exact solution except for 21 extra colored cells in the front. After a full rotation, the total number of colored cells increases a mere 8%, from 961 to 1033. The initial peak value (1000 unit) is reduced by about 5% ($C_{\mathrm{mx}} = 946$ unit) after one cycle and the full-cycle NRMS error for the UNO3 scheme on the SMC 1° grid is 0.0228. Note that the NRMS error at 90° rotation (0.0358) is even larger than the full cycle value. This reflects an extra error introduced by the resolution disparity. Because the number of cells representing the cosine bell varies with position on the sphere (961 on the equator and 1531 at the pole), the simulated bell is, in effect, being compared to different ''exact'' solutions at different positions due to the changing resolution.

The impacts of the spatial resolution on the NRMS error are clearly revealed by the time series of the error norms shown in Fig. 5e. The NRMS defined by Eq. (6) is identical to the l_2, one of three error norms used by Williamson et al. (1992) and other authors. The other two error norms are the normalized mean absolute error (l_1) and the normalized maximum absolute error (l_∞). For the cosine bell test, l_∞ is the relative error of the bell peak or within a grid box of the bell peak. Also, for nonoscillatory schemes, the l_1 error does not differ much from the NRMS error. The NRMS error increases in the first quarter cycle and reaches a local maximum at 90° rotation. The 90° NRMS value shown in Fig. 5d (0.0358) is the local maximum NRMS value. After its 90° maximum, the NRMS error decreases to a local minimum at about 140° rotation. The error peaks again at 270° and

TABLE 5. Error norms after 1 full cycle for the cosine bell rotation tests using the UNO2 scheme on the SMC 1° grid and the UNO3 scheme on the SMC 1° and 2° grids. Error norms by other authors are also listed here but only as an approximate guide.

	$\alpha = \pi/2$ (l_1, l_2, l_∞)	$\alpha = \pi/2$–0.05 (l_1, l_2, l_∞)	$\alpha = 0$ (l_1, l_2, l_∞)
SMC 1° UNO2	0.1777, 0.1443, 0.1949	0.1777, 0.1451, 0.2055	0.0576, 0.0501, 0.0658
SMC 1° UNO3	0.0196, 0.0228, 0.0531	0.0201, 0.0233, 0.0600	0.0090, 0.0116, 0.0235
SMC 2° UNO3	0.1220, 0.1122, 0.1650	0.1211, 0.1124, 0.1777	0.0457, 0.0449, 0.0697
WAF-AMR (HN03)	0.1296, 0.1320, 0.1794	0.1298, 0.1308, 0.1792	0.0572, 0.0523, 0.0572
SLICE-S (ZWS04)	0.079, 0.049, 0.042	0.079, 0.048, 0.039	0.046, 0.029, 0.022
CCS-P (NSS02)	0.051, 0.041, 0.065	0.055, 0.043, 0.064	0.036, 0.034, 0.042

450° as shown in Fig. 5e, indicating a period of 180° rotation. These periodic peaks of the NRMS error imply that they are caused by the spatial resolution disparity between the polar and equatorial regions. The resolution error disappears once the bell reaches a location of the same resolution as its initial location (of 180° rotation period), resulting in a reduction of the NRMS error.

Note that errors incurred by numerical diffusion never decrease with time because diffusion is an irreversible process. The NRMS error curve shown in Fig. 5e may be interpreted as a superposition of the periodic resolution error and the steadily increasing diffusion error. In subsequent cycles, the resolution error becomes less prominent as the diffusion error accumulates and eventually exceeds the resolution error. The error time series for the SMC 2° case (not shown) also has a peak at 90° rotation and decreases by a small amount after 90°. But the numerical diffusion on the SMC 2° grid is so large that it exceeds the resolution error within one cycle. The resolution disparity error is confirmed by another test with the initial bell at the South Pole (SP test), again with $\alpha = \pi/2$. As in the previous test, the NRMS error for the SP test peaks at 90° rotation (i.e., when the bell is on the equator), and it reaches a local minimum when the bell is near the North Pole. Subsequent rotations in the SP test show 180° periodic error peaks similar to those in Fig. 5e except that the peaks correspond to bell positions on the equator.

The error peaks caused by the ''exact solution'' discretized at different spatial resolutions should be avoided for the assessment of the simulation because they are not real errors caused by the simulation. Error norms are better evaluated at a resolution that is the same as the initial one. So the 1-cycle error norms are good indicators of the simulation errors. The 1-cycle (360°) error norms for the cosine bell tests are given in Table 5. Since the UNO2 scheme is more diffusive than the UNO3 scheme, the errors for UNO2 are expected to be larger than those for UNO3. This is confirmed by the error norms for the two schemes on the SMC 1° grid (second and third rows in Table 5). The error norms for the UNO3 scheme on the two SMC grids can be used to assess the effects of spatial resolution. The errors on the SMC 2° grid (fourth row) are obviously larger than those on the SMC 1° grid (third row). Note that the errors for the UNO3 scheme on the SMC 2° grid are comparable to those for the UNO2 scheme on the SMC 1° grid, indicating that halving the grid length is nearly equivalent to replacing the UNO2 with the UNO3 scheme.

Also listed in Table 5 are some published results: the SLICE-S scheme (ZWS04), the weighted average flux (WAF) scheme (HN03), and the positive-definite version of the conservative cascade scheme (CCS-P) by Nair et al. (2002, hereafter NSS02). Like the UNO schemes, the WAF scheme (HN03) is a finite-volume scheme, while SLICE-S (ZWS04) and CCS-P (NSS02) are SL schemes. It has to be emphasized that the results from these three schemes are not directly comparable to the SMC grid results due to differences in grid resolutions and between the Eulerian and SL schemes. These results are provided here only as an approximate guideline on the quality of the Eulerian and SL schemes for the same polar transport task.

Note that all three cited results are on the standard 64 × 128 latitude–longitude grid. Although this grid is on average coarser than the SMC 2° grid, it has a much higher polar resolution (over 2 times) than the SMC 2° grid. For instance, if the same cosine bell [Eq. (9)] is mapped onto the standard 64 × 128 grid, its non-0 cell number will be about 145 on the equator and 896 at the pole (over 6 times). The SMC 2° grid has a much smaller polar-to-equatorial ratio, $371/247 \sim 1.5$. Based on average resolution, the SMC 2° grid is quite close to the standard 64 × 128 grid for comparison. As shown in Table 5, all error norms of the UNO3 scheme on the SMC 2° grid are smaller than the WAF ones except for the l_∞ in the $\alpha = 0$ case, where the UNO3 l_∞ norm (0.0697) is slightly larger than the WAF value (0.0572). The SL schemes (SLICE-S and CCS-P) on the standard 64 × 128 grid perform better than the UNO3 scheme on the SMC 2° grid, implying that they are more accurate than the UNO3 scheme. However, higher accuracy may be achieved by increasing spatial resolution. For instance, the UNO3 scheme on the SMC 1° grid outperforms any of the three published schemes on the standard grid as measured by the NRMS error.

5. SMC grid for the ocean surface

The advantage of the unstructured SMC grid manifests itself most clearly when some cells are removed from the full global grid. A global ocean surface wave model SMC grid is designed so that the size-1 cells are exactly the same as the 40-km global latitude–longitude grid ($\Delta\varphi = 0.375°$ and $\Delta\lambda = 0.5625°$) of one Met Office ex-operational atmospheric model, which provided surface wind forcing for the global wave model. As with the previous SMC grids, the polar regions have been replaced by merged cells, including a polar cell centered at the North Pole. All cells on land have been removed as they are not needed in the ocean surface wave model. Although areas of ice-covered ocean surface are usually treated as land in the wave model, here cells in the Arctic region are retained for illustration. There are 167 944 sea cells in total, which is about 55% of the cell count of the conventional grid (480 × 640). This massive reduction in cell count implies that, per time step, transport on the SMC grid will cost much less than on the full latitude–longitude grid. If the fact that a larger time step can be used with the SMC grid is also taken into account, then transport on the SMC grid will be even faster than on the conventional grid.

Another feature of the SMC grid is the unification of the boundary conditions with the internal flux evaluation. Cell faces at the coastline are assumed to be bounded by two consecutive empty (zero) cells. Thus, any wave energy transported into these zero cells will disappear, and no wave energy will be injected out of these zero cells into any sea cells. This convenient setup conforms to the zero wave energy boundary condition at land points used by ocean surface wave models (e.g., Tolman et al. 2002) and allows all the boundary cell faces to be treated in the same way as internal faces. If other boundary conditions are to be used, the pointers to the cells just outside the boundary cell faces must be changed accordingly. For instance, the zero-gradient boundary condition can be implemented by setting the pointer to the cell just outside the boundary face equal to the pointer to the cell just inside the face. Predetermined boundary conditions can be implemented by adding extra cells outside the boundaries.

An additional benefit of using two consecutive zero-boundary cells is the complete blocking of wave energy by single-point islands. On a conventional grid, wave energy can ''leak'' through a single-point island due to the interpolation with neighboring sea points in transport schemes that use a five-point stencil like the UNO schemes. At SMC grid boundary faces, any single-point island is extended into two zero cells beyond its boundary face. As a result, wave energy cannot pass through such islands with the UNO schemes, which use the UCD cells for interpolation. Some small islands in the Mediterranean and eastern Pacific are visible as single-point islands in the SMC 40-km grid shown in Fig. 6. Their blocking effect is demonstrated in the following SSF rotation test.

Here, the test is restricted to a single wave energy spectral component, or a scalar variable. Each ocean wave spectral component travels in a fixed direction (i.e., along great circles) at a constant speed in deep water (over ~200 m). For demonstration purposes, the solid-body rotation field defined in Eq. (5) with $\varphi_P = 0$ and $\lambda_P = \pi$ will be used in the following ocean surface SMC grid test. The rotational pole is on the equator in the middle of the Pacific. The angular speed ω is set to $10°\ \mathrm{h}^{-1}$ as in the previous SSF rotation tests, but a smaller time step of 90 s is used. The maximum Courant number is 0.840. A full cycle around the globe then takes 1440 time steps. The SSF is applied with the initial conditions by setting those sea points within a stripe 12° wide along the equator to 5 units and the rest sea points to 1 unit. The initial SSF conditions are shown in Fig. 6a, and the cell value range is indicated by the minimum ($C_{\min} = 1.0$) and maximum ($C_{\max} = 5.0$) values. The white regions represent land, and small islands are clearly visible by contrast to the SSF colors. The rotational poles are marked by the small N in the Pacific and S in the South Atlantic on the initial equatorial stripe. The N or S letter represents exactly one cell size and is almost illegible on this scale. The same color keys as in the previous SSF rotation tests are used.

Figure 6b shows the transported field after a 10° rotation ($t = 1$ h) with the UNO3 scheme. The dark shadow (unfilled cells to show the grid mesh) downstream of coastlines indicate zero wave energy values as no wave energy comes out of the coastlines. The complete blocking of wave energy by islands is clearly visible by the dark shadows downstream of them, including those single-point islands. The edges of the raised stripe are rounded down by the implicit numerical diffusion, resulting in a transition zone in intermediate colors. Cell values upstream of coastlines remain at their initial values as wave energy transported into the coastlines simply disappears (no reflection). The unclipped background and the stripe's top remain uniformly flat everywhere, including in the Arctic. This result indicates that advection on the ocean surface SMC grid with the UNO3 scheme is smooth, including through the polar cell, across the size-changing parallels, and into coastlines. Note that the maximum value at $t = 1$ h is slightly increased to

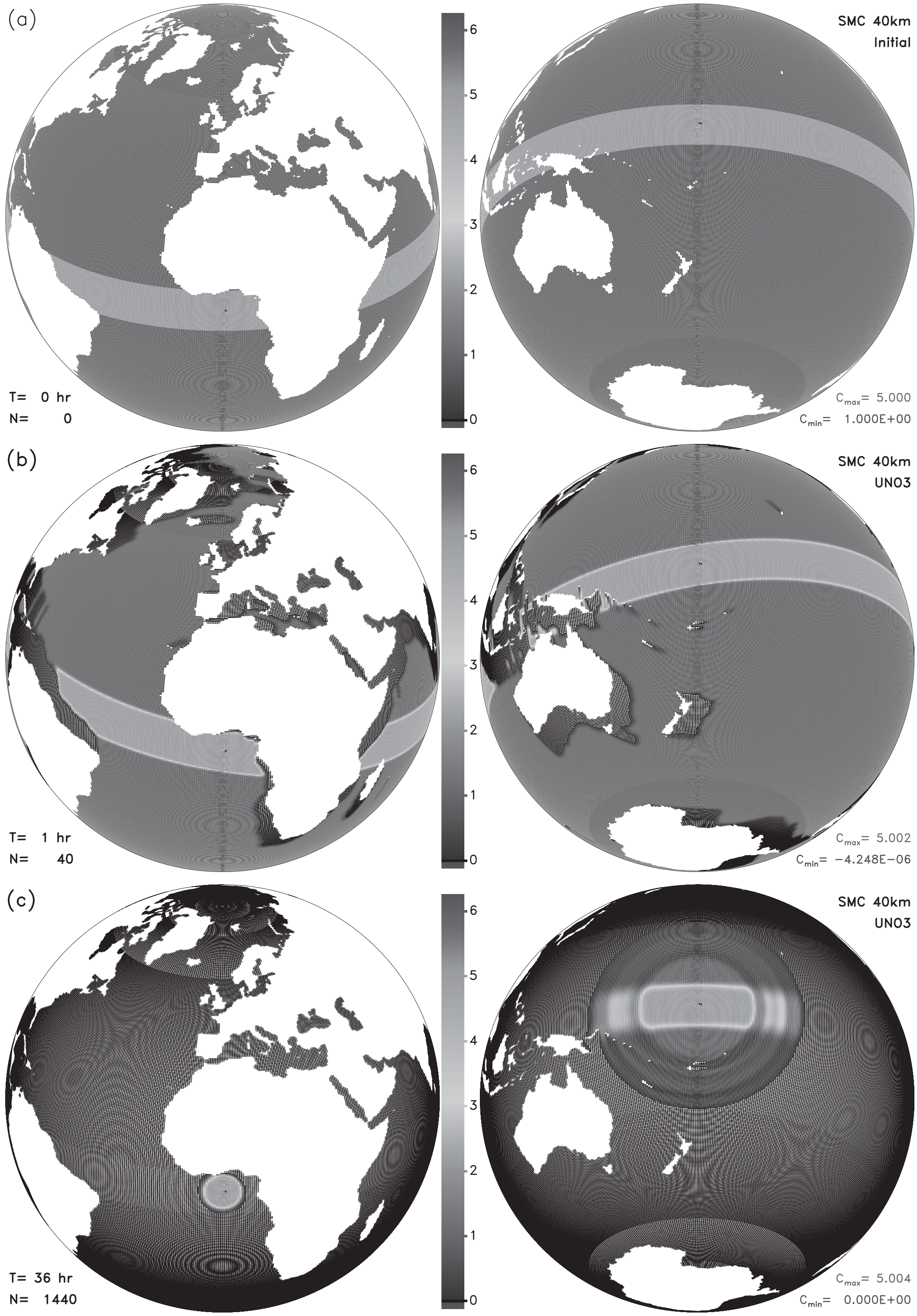

FIG. 6. Solid-body rotation of the spherical step function with the UNO3 scheme on a global ocean surface SMC 40-km grid, including the whole Arctic Ocean. The rotational north pole is at 180° on the equator (denoted by the small N), and the rotation angular speed is 10° h^{-1}.

5.002 and the minimum value is a small negative value of -4.248×10^{-6}. This is in agreement with the previous results for the SMC 1° grid and confirms that the UNO3 scheme generates very small oscillations on the spherical grid. These small negative values could be removed by applying a simple positive filter. Such filters are used in ocean wave models (Golding 1983; Tolman et al. 2002) to ensure that wave energy remains nonnegative. These filters can also be used for nonnegative fields in other models.

Figure 6c shows the remaining SSF after a full cycle or 360° rotation ($t = 36$ h) with the UNO3 scheme on the ocean surface SMC 40-km grid. By this time, most of the initial SSF field has been clipped out by the coastlines, leaving only one round disk on each hemisphere. For this reason, it is no longer meaningful to evaluate the NRMS error with reference to the initial conditions. The surviving section of the stripe retains its initial value of 5 units except for the rounded edges. The eastern disk (in the right panel of Fig. 6c) has passed through several islands, incurring some grooves downstream of the islands. As they rotate away from the islands, these grooves are gradually filled up by numerical diffusion. The maximum value becomes 5.004 and the minimum value is now 0 at double precision (64 bits). So the small oscillation is only about 0.1%. These results are satisfactory for ocean surface wave energy transport.

A similar SSF rotation test has been performed with the UNO2 scheme. The result is quite similar to the one with UNO3 except that the numerical smoothing in the UNO2 case is more prominent. This is manifested by an enlarged transition zone at the unclipped stripe edges and around the margin of the remaining disks. The shadow grooves downstream of small islands are shorter in the UNO2 case because of the enhanced numerical diffusion. Nevertheless, the UNO2 scheme is accurate enough for ocean surface wave models because a strong explicit smoothing term, larger than the Dif2 implicit numerical diffusion term described in Li (2008), is required in ocean wave models to control the so-called garden sprinkler effect due to the discrete spectral directions (Tolman 2002). The strong smoothing term makes the final wave energy fields generated by the UNO2 and UNO3 schemes almost indistinguishable. Experience at the Met Office has shown that switching to the UNO2 scheme from the ULTIMATE QUICKEST third-order advection scheme (Leonard 1991) in the WAVEWATCH III model (Tolman et al. 2002) has saved about 30% in advection computing time without any loss of accuracy in ocean wave energy transport. If the SMC grid is implemented in this wave model, further savings on advection are expected. So the UNO2 scheme on this SMC grid should be ideal for global ocean surface wave models. The UNO3 scheme can be used in models in which large numerical diffusion is not required.

To extend ocean surface wave models to high latitudes, one remaining difficulty is the local eastern reference direction used to define the directional components of wave spectra. The increased curvature of the parallels at high latitudes renders the scalar assumption of the directional components invalid near the North Pole. The zonal direction change of a given spectral bin becomes too large to be ignored within one time step. The difficulty stems from the choice of the local eastern direction as the spectral reference direction. This is, however, not necessary in the Arctic, and the problem can be solved by simply introducing a fixed reference direction for the Arctic region. The unstructured feature of the SMC grid allows this to be done conveniently by using a different reference direction in the Arctic region from the rest of the model domain and linking the two regions with some extra boundary cells. Numerical results confirm that the SMC grid with a fixed reference direction in the Arctic can be used to extend a global wave model to high latitudes and can even include the North Pole (Li 2009). The approach of using a fixed reference direction to define vector components in polar regions may also be applicable in dynamical models that use reduced grids. This is, however, beyond the scope of this paper.

6. Summary and conclusions

Second- and third-order upstream nonoscillatory (UNO) advection schemes are applied on a spherical multiple-cell (SMC) grid for global transport. As with the reduced grid, the SMC grid relaxes the CFL restriction on the Eulerian advection time step on the conventional latitude–longitude grid by zonally merging cells toward the poles. Round polar cells are introduced to remove the singularity of the standard latitude–longitude grid at the poles. The mapping between the conventional latitude–longitude grid and the SMC grid is straightforward. Spherical step function (SSF) rotation tests are used to demonstrate global transport on the SMC grid and to compare this with transport on the standard latitude–longitude and reduced grids. Cosine bell solid-body rotation and deformation flow tests are used to compare the UNO schemes on the SMC grid with other transport schemes. The unstructured feature of the SMC grid allows unused (i.e., land) cells to be removed from the advection calculation and from memory. Application of the SMC grid on the global ocean surface is used to demonstrate the flexibility of the SMC grid by removing all land points, significantly reducing both memory and computing cost in global ocean surface wave models. In response to retreating Arctic sea ice, a fixed reference direction for definition of wave spectra at high latitudes is recommended to extend ocean surface wave models into the whole Arctic on the SMC grid.

Numerical results indicate that the UNO3 scheme on the SMC grid is efficient for global transport. Although it generates errors slightly larger than some advanced semi-Lagrangian schemes at roughly the same spatial resolution, its accuracy can be improved by increasing the resolution. The SMC 1° and 2° grids are used to illustrate the spatial resolution effect. The UNO2 scheme is fast and accurate enough for models in which large numerical diffusion is required, such as in ocean surface wave models. The UNO schemes are easy to implement on the SMC grid because this grid uses the same rectangular stencil as the conventional latitude–longitude grid, allowing finite-difference schemes to be used directly. The UNO schemes on the SMC grid are recommended for global atmospheric and oceanic tracer transport.

Acknowledgments. The author is grateful to Drs. Nigel Wood and Andrew Saulter (Met Office) and the three anonymous reviewers for their useful comments that improved the content and language.

REFERENCES

Allen, D. J., A. R. Douglass, R. B. Rood, and P. D. Guthrie, 1991: Application of a monotonic upstream-biased transport scheme to three-dimensional constituent transport calculations. *Mon. Wea. Rev.,* **119,** 2456–2464.

Berger, M., and J. Oliger, 1984: Adaptive mesh refinement for hyperbolic partial differential equations. *J. Comput. Phys.,* **53,** 484–512.

Golding, B. W., 1983: A wave prediction system for real-time sea state forecasting. *Quart. J. Roy. Meteor. Soc.,* **109,** 393–416.

Hanert, E., D. Y. Le Roux, V. Legat, and E. Deleersnijder, 2004: Advection schemes for unstructured grid ocean modelling. *Ocean Modell.,* **7,** 39–58.

Hubbard, M. E., and N. Nikiforakis, 2003: A three-dimensional, adaptive, Godunov-type model for global atmospheric flows. *Mon. Wea. Rev.,* **131,** 1848–1864.

Jablonowski, C., M. Herzog, J. E. Penner, R. C. Oehmke, Q. F. Stout, B. van Leer, and K. G. Powell, 2006: Block-structured adaptive grids on the sphere: Advection experiments. *Mon. Wea. Rev.,* **134,** 3691–3713.

——, R. C. Oehmke, and Q. F. Stout, 2009: Block-structured adaptive meshes and reduced grids for atmospheric general circulation models. *Philos. Trans. Roy. Soc.,* **367A,** 4497–4522.

Janssen, P., 2004: *The Interaction of Ocean Waves and Wind*. Cambridge University Press, 300 pp.

Kageyama, A., and T. Sato, 2004: The ''yin–yang grid'': An overset grid in spherical geometry. *Geochem. Geophys. Geosyst.,* **5,** Q09005, doi:10.1029/2004GC000734.

Killworth, P. D., J. G. Li, and D. Smeed, 2003: On the efficiency of statistical assimilation techniques in the presence of model and data error. *J. Geophys. Res.,* **108,** 3113, doi:10.1029/2002JC001444.

Kurihara, Y., 1965: Numerical integration of the primitive equations on a spherical grid. *Mon. Wea. Rev.,* **93,** 399–415.

Leonard, B. P., 1991: The ULTIMATE conservative difference scheme applied to unsteady one-dimensional advection. *Comput. Methods Appl. Mech. Eng.,* **88,** 17–74.

——, A. P. Lock, and M. K. MacVean, 1996: Conservative explicit unrestricted-time-step multidimensional constancy-preserving advection schemes. *Mon. Wea. Rev.,* **124,** 2588–2606.

Li, J. G., 2003: A multiple-cell flat-level model for atmospheric tracer dispersion over complex terrain. *Bound.-Layer Meteor.,* **107,** 289–322.

——, 2008: Upstream nonoscillatory advection schemes. *Mon. Wea. Rev.,* **136,** 4709–4729.

——, 2009: Spherical multiple-cell grid to include the Arctic in global ocean wave model. *Proc. 11th Int. Workshop on Wave Hindcasting and Forecasting,* Halifax, NS, Canada, WMO/IOC Joint Technical Commission for Oceanography and Marine Meteorology (JCOMM). [Available online at http://www.waveworkshop.org/11thWaves/index.htm.]

Li, X., D. Chen, X. Peng, K. Takahashi, and F. Xiao, 2008: A multimoment finite-volume shallow-water model on the yin–yang overset spherical grid. *Mon. Wea. Rev.,* **136,** 3066–3086.

Li, Y., and J. S. Chang, 1996: A mass-conservative, positive-definite, and efficient Eulerian advection scheme in spherical geometry and on a nonuniform grid system. *J. Appl. Meteor.,* **35,** 1897–1913.

Lipscomb, W. H., and T. D. Ringler, 2005: An incremental remapping transport scheme on a spherical geodesic grid. *Mon. Wea. Rev.,* **133,** 2335–2350.

McDonald, A., and J. R. Bates, 1989: Semi-Lagrangian integration of a gridpoint shallow water model on the sphere. *Mon. Wea. Rev.,* **117,** 130–137.

Nair, R. D., and B. Machenhauer, 2002: The mass-conservative cell-integrated semi-Lagrangian advection scheme on the sphere. *Mon. Wea. Rev.,* **130,** 649–667.

——, J. Cote, and A. Staniforth, 1999: Cascade interpolation for semi-Lagrangian advection over the sphere. *Quart. J. Roy. Meteor. Soc.,* **125,** 1445–1468.

——, J. S. Scroggs, and F. H. M. Semazzi, 2002: Efficient conservative global transport schemes for climate and chemistry models. *Mon. Wea. Rev.,* **130,** 2059–2073.

Prather, M. J., M. McElroy, S. Wofsy, G. Russel, and D. Rind, 1987: Chemistry of the global troposphere: Fluorocarbons as tracers of air motion. *J. Geophys. Res.,* **92,** 6579–6613.

Purser, R. J., and M. Rancic, 1997: Conformal octagon: An attractive framework for global models offering quasi-uniform regional enhancement of resolution. *Meteor. Atmos. Phys.,* **62,** 33–48.

Rasch, P. J., 1994: Conservative shape-preserving two-dimensional transport on a spherical reduced grid. *Mon. Wea. Rev.,* **122,** 1337–1350.

Ritchie, H., 1987: Semi-Lagrangian advection on a Gaussian grid. *Mon. Wea. Rev.,* **115,** 608–619.

Robert, A., T. L. Yee, and H. Ritchie, 1985: A semi-Lagrangian and semi-implicit numerical integration scheme for multilevel atmospheric models. *Mon. Wea. Rev.,* **113,** 388–394.

Roe, P. L., 1985: Some contributions to the modelling of discontinuous flows. *Large-Scale Computations in Fluid Mechanics,* E. Engquist, S. Osher, and R. J. C. Sommerville, Eds., Lectures in Applied Mathematics, Vol. 22, American Mathematical Society, 163–193.

Sadourny, R., 1972: Conservative finite-difference approximations of the primitive equations on quasi-uniform spherical grids. *Mon. Wea. Rev.,* **100,** 136–144.

Takacs, L. L., 1985: A two-step scheme for the advection equation with minimized dissipation and dispersion errors. *Mon. Wea. Rev.,* **113,** 1050–1065.

Tolman, H. L., 2002: Alleviating the garden sprinkler effect in wind wave models. *Ocean Modell.,* **4,** 269–289.

——, B. Balasubramaniyan, L. D. Burroughs, D. V. Chalikov, Y. Y. Chao, H. S. Chen, and V. M. Gerald, 2002: Development and implementation of wind-generated ocean surface wave models at NCEP. *Wea. Forecasting,* **17,** 311–333.

WAMDI group, 1988: The WAM model—A third generation ocean wave prediction model. *J. Phys. Oceanogr.,* **18,** 1775–1810.

Williamson, D. L., and G. L. Browning, 1973: Comparison of grids and difference approximations for numerical weather prediction over a sphere. *J. Appl. Meteor.,* **12,** 264–274.

——, J. B. Drake, J. J. Hack, R. Jakob, and P. N. Swarztrauber, 1992: A standard test set for numerical approximations to the shallow-water equations in spherical geometry. *J. Comput. Phys.,* **102,** 221–224.

Zerroukat, M., N. Wood, and A. Staniforth, 2004: SLICE-S: A Semi-Lagrangian inherently conserving and efficient scheme for transport problems on the sphere. *Quart. J. Roy. Meteor. Soc.,* **130,** 2649–2664.